POLITECNICO DI TORINO
Repository ISTITUZIONALE

Multiphysics Simulation of a Superconducting Neutron Detector

Original
Multiphysics Simulation of a Superconducting Neutron Detector / Sparacio, S., Celentano, G., Pietropaolo, A., Torsello, D., Laviano, F.. - In: IEEE TRANSACTIONS ON APPLIED SUPERCONDUCTIVITY. - ISSN 1051-8223. - 35:3(2025), pp. 1-6. [10.1109/tasc.2024.3504844]

Availability:
This version is available at: 11583/2995266 since: 2024-12-12T15:17:53Z

Publisher:
Institute of Electrical and Electronics Engineers

Published
DOI:10.1109/tasc.2024.3504844

Terms of use:

This article is made available under terms and conditions as specified in the corresponding bibliographic description in the repository

Publisher copyright

(Article begins on next page)

26 November 2026

Multiphysics Simulation of a Superconducting Neutron Detector

Simone Sparacio, Giuseppe Celentano, Antonino Pietropaolo, Daniele Torsello, *Member, IEEE*, and Francesco Laviano

***Abstract*—The detection of neutrons is crucial for both the operation of nuclear devices and the development of advanced imaging techniques. Recently, a hybrid superconducting niobium-boron sensor on a Si/SiO_2 substrate has been developed, aiming for high pulse shape discrimination and controllability of the relaxation time. This device detects thermal neutrons by leveraging the ^{10}B(n,α)^{7}Li reaction in the B layer and the interaction of the charged products with the Nb strip. To critically assess the operation of the Nb-B thermal neutron detector, a multiphysics modeling approach is presented here. The software COMSOL Multiphysics is used to provide thermal and electrical responses of this device during the transition-to-normal state and its recovery phase. The study takes into account the impact of the thermal irradiation of the cryostat lid and the joule heating on the operating conditions of the Nb strip. Moreover, a pulsed heat load is introduced in the model to simulate the energy released by either the α or the Li reaction products in the current-biased Nb strip. The SRIM software is used to obtain the deposited power density profiles and their mean volume of interaction within the sample. For simplicity, the reaction is assumed to take place at the half-thickness of the B layer and the particles propagate perpendicularly to the sample surface. Finally, an iterative procedure was applied to find the most favorable conditions to employ the device in a self-recovering mode by varying both the bias current and the cold finger temperature. This study presents a comprehensive understanding of the working mechanism of the Nb-B thermal neutron detector and proposes a computational approach to find the optimal working point of superconducting neutron detectors.**

***Index Terms*—FEM, multiphysics simulation, niobium, superconducting neutron detector, superconducting sensor.**

I. Introduction

NEUTRON detection technology has been actively developed for almost a century (a comprehensive review can be found in [1]), and superconducting neutron detectors were introduced Drukier et al. [2], who suggested to use a superheated superconducting colloid (SSC). This consisted of sedimented spherical grains of indium on a parafine wax, loaded with a natural boron compound, B_4C. Although different superconducting detector configurations, such as superconducting tunneling junctions (STJ), transition-edge sensors (TES)/Bolometers, and kinetic inductance detectors (KID), have been developed in the meantime for photons and charged particle detection, the SSC (see also [3], [4]) was the only one used for neutrons until 2003. In the same year, Takahashi et al. [5] designed the first neutron TES prototype using the novel MgB_2 superconductor on a sapphire substrate. A meander line layout was proposed with a dc voltage bias and considering the nuclear reaction ^{10}B(n,α)^{7}Li directly in the MgB_2. In addition, Machida et al. [6] performed a numerical simulation, based on the time-dependent Ginzburg–Landau equation coupled with the Maxwell and heat diffusion equations, on a current-biased MgB_2 film. They found a threshold width of about 40ξ ($T = 0$) above which the neutral particle could not be detected since the normal region did not spread enough to break the wire electromagnetic symmetry. Between 2007 and 2012, Ishida et al. [7], [8], [9] and Machida et al. [10], [11], [12], [13] performed, respectively, experimental and numerical evaluations on the thermal response and on the charged density profile of a microfabricated MgB_2 meander line on Si/SiN/SiO substrate and with different electrodes (i.e., Al and Nb). They claimed the ability of this device to count events at a rate much faster than 10^6 events/s due to its very fast dynamics (t $<$ 1 μs). Moreover, they investigated the spatial dependence of the signal amplitude across the strip line and found a carrier imbalance due to a spin imbalanced superconductor confinement. An extensive research on TES for thermal neutron detection was also performed in the period 2015–2018 by Merlo et al. [14], [15], [16], [17]. Their experimental progresses were first centered on a current-biased Nb superconducting strip and then on a NbN one on a silicon buffer and coated by a boron layer. The steep dR/dT curve of these materials near the critical temperature, T_c, lead to a readable superconducting-to-normal transition even with a small temperature increment. Shishido and co-workers, presented a similar device (i.e., a Nb-based meander line of 64 strips of 1μm width and 40 nm thick) using a current biased kinetic inductance approach, which allowed a wider I-T region operation preserving

Received 30 September 2024; revised 20 November 2024; accepted 20 November 2024. Date of publication 21 November 2024; date of current version 21 February 2025. This work was supported in part by the Ministry of Education, Universities and Research through the "Programma Operativo Nazionale (PON) Ricerca e Innovazione 2014–2020," in part by the Italian Ministry of Foreign Affairs and International Cooperation under Grant US23GR16, and in part by Eni S.p.A. *(Corresponding author: Simone Sparacio.)*

Simone Sparacio, Daniele Torsello, and Francesco Laviano are with the Department of Applied Science and Technology, Politecnico di Torino, and INFN - Sez. Torino, 10125 Torino, Italy (e-mail: simone.sparacio@polito.it).

Giuseppe Celentano is with Superconductivity Laboratory, ENEA, 00044 Frascati, Italy.

Antonino Pietropaolo is with Nuclear Technologies Laboratory, ENEA, 00044 Frascati, Italy.

Color versions of one or more figures in this article are available at https://doi.org/10.1109/TASC.2024.3504844.

Digital Object Identifier 10.1109/TASC.2024.3504844

© 2024 The Authors. This work is licensed under a Creative Commons Attribution 4.0 License. For more information, see https://creativecommons.org/licenses/by/4.0/

TABLE I
COMPARISON OF NEUTRON DETECTOR ARCHITECTURES

Architecture	Time resol. [μs]	Spatial resol. [μm]	Efficiency	Rate capab. [MHz]	Ref.
Gas-filled Detectors (e.g., ^{3}He, and ^{10}B tubes)	1	1–10^3	Moderate-high for thermal neutron Very low for fast neutron	10^{-3}	[37]–[39]
Scintillator Detectors (e.g., ZnS/^{6}Li with LiF, Li-glass, and plastic scintil.)	10^{-3}	10^3	High for thermal neutrons Moderate for fast neutron	1	[40]–[41]
Solid-State Detectors (e.g., Silicon, ^{10}B, or ^{6}Li thin-film detectors)	10^{-6}–10^{-3}	10^3	Low-moderate for both thermal and fast neutrons	1	[42]–[43]
Proportional Counters and Multi-wire Proportional Chambers (MWPCs)	1	10^3	Moderate-high for thermal neutrons Low for fast neutron	10^{-3}	[44]
Semiconductor-based Detectors (e.g., Diamond detectors)	10^{-3}	10^3	Low for thermal neutrons Moderate for fast neutron	1	[45]–[46]
Neutron-sensitive CCD/CMOS-based detectors	1–10^3	1	Low-moderate for thermal neutrons Very low for fast neutron	10^{-6}	[47]
Superconducting Neutron Detectors (STJs, SNSPDs)	10^{-6}–10^{-3}	10^{-3}–1	High for thermal neutrons Moderate-high for fast neutron	1	[48]

the high-speed detection. The authors in [18], [19], [20], [21], [22], [23], [24], [25], [26], [27], [28], [29], [30], [31], [32], [33], and [34] demonstrated its operability with a detection range of tens of ns. This resulted in the identification of single neutrons but also time-dependent particle fluxes, their impact position, and the temperature dependence of the signal. The last developments on superconducting neutron detection schemes came from Brock et al. [35], [36], whom in 2023 presented the first high-temperature CB-TES based on $YBa_2Cu_3O_{7-x}$ meander line, deposited on a metallic substrate and covered by 4-μm-thick B_4C [36]. Despite their shorter and heterogeneous historical development, superconducting neutron detectors offer high time resolution, exceptional spatial resolution, high efficiency for thermal neutrons, and high rate capability, with respect to other neutron detectors. A quick overview of the capability ranges of the different architectures is reported in Table I.

In this research, starting from the experimental apparatus described in [14], we present a 3-D multiphysics simulation of the sensor and its operating environment, devoting our attention on the effective operating temperature following the surface-to-surface radiation with the 80 K cryostat thermal-screen walls and the Joule heating produced by the resistive transport current during operation. We then studied the spatial and the temporal evolution of the device temperature, the electric field, and the current density distribution during the particle detection, validating the model with the experimental results and estimating the relative figure of merits. Finally, based on this validated setup, we found an experimentally feasible combination of bias current and operation temperature that allows the self-recovery of the superconducting state after neutron detection without the need to shunt the device or to externally interrupt the bias current.

II. EXPERIMENTAL SETUP AND CONSIDERATIONS

The detector was created using lift-off techniques, depositing a 150-nm-thick layer of Nb on a 1 $\times$ 1 cm^2 silicon wafer with a 1-μm-thick SiO_2 surface layer. On top of the patterned Nb strip, 450 nm of natural boron was deposited using e-beam evaporation. In the boron layer, the absorption reaction produces a 1.5 MeV alpha particle and a 0.8 MeV lithium particle with opposite momenta. This means that either the alpha or the lithium particle will strike the microstrip for each neutron conversion. The sample was mounted at the end of an actively cooled cryostat using ^{4}He, and the V-I and V-t measurements were performed on the INES beam-line at the ISIS pulsed neutron source in the Rutherford-Appleton Laboratory in the U.K. A photograph of the experimental scheme is reported in the left panel of Fig. 1 while the top part of Fig. 2 shows the V-t measurement for a sample with a width of 10 μm and a length of 600 μm, biased with a current of 4.5 mA, at the operating temperature of 8.12 K.

The interaction of the reaction products with the device materials heats a section of the wire (approximately a cylinder with radius equal to the mean particle lateral deviation in Nb) to above the superconducting transition temperature. The bias current avoids the normal region, increasing its density in the remaining width of the wire, and eventually triggering a quench. As the joule heating spreads across the wire, the temperature increment due to the steep transition, dR/dT, is converted to a larger, local, increase in the resistance of the superconductor. This change of resistance can then be measured by intercepting the voltage across the wire length, as a proof of particle detection.

III. NUMERICAL MODELING

A detailed 3-D electro-thermal model of the cryogenic head is implemented on COMSOL Multiphysics [49]. In Fig. 1 the frontal and the top view of the simulated domain is reported. Because of the high aspect ratio between the sample and the other components, a *layered shell approximation* is adopted for the sample in both the thermal end the electrical analysis. The coupling term between the two physics are the joule heating and the temperature dependent properties.

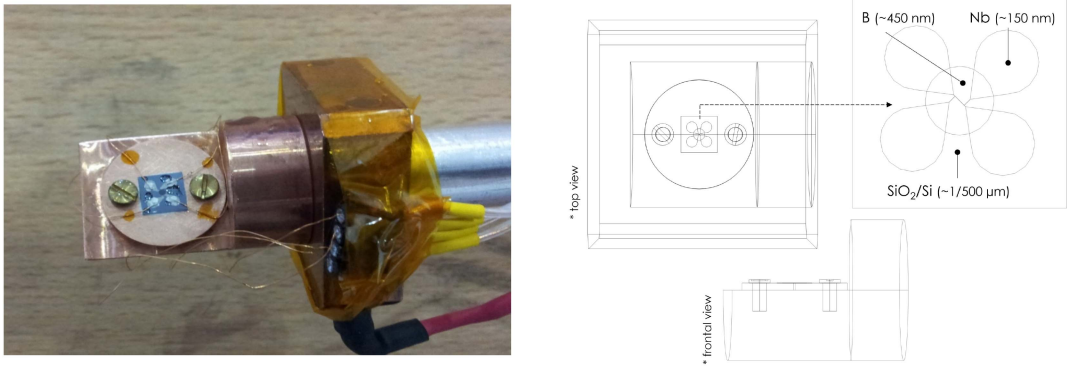

Fig. 1. Left panel: photograph of the sample–from the top: boron (dark blue), niobium (light blue), Si/SiO_2 substrate (blue)–sample holder, and cold finger. Right panel: frontal and top schematic view of the cryostat head, with the cold finger end, the screws, the sample holder, and the detail of the sample.

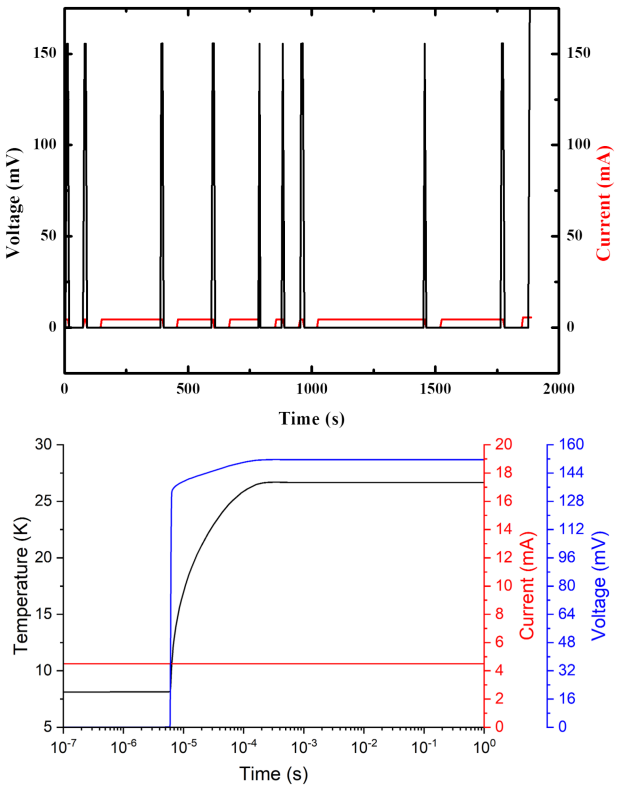

Fig. 2. Upper panel: experimental V-t measurements an biased current. Lower panel: simulated V-t data (blue), biased current (red), and average temperature of the Nb microstrip between the voltage contacts (black).

A. Thermal Model

The temperature profile is solved both in time and space by means of the classical Fourier equation, as reported in (1). The analysis considers both the energy contribution of the particle collision and the Joule losses, and particular attention is also devoted to the effects of the surface-to-surface radiation between the cryostat thermal shield at 80 K and the internal surfaces

$$\rho C_p \frac{\partial T}{\partial t} + \nabla_t \cdot (-k (\nabla_t T + \nabla_n T)) = Q$$
$$Q = Q_p + Q_J + Q_{irr}. \tag{1}$$

Here, $\rho, C_p,$ and k are, respectively, the density, the specific heat, and the thermal conductivity of each material. ∇_t and ∇_n are the tangential and the normal component of the spatial derivative in the thin shell approximation. Q is the sum of the heat released by the traversing charged particle, Q_p, the electromagnetic heating, $Q_J = E \cdot J$, and the thermal irradiation, $Q_{irr} = \epsilon\sigma(T_{\text{ref}}^4 - T^4) \cdot A/V$, from the surrounding surfaces. In the latter, ϵ is the material thermal emissivity, $\sigma = 5.67 \times 10^{-8}[\text{Js}^{-1}\text{m}^2\text{K}^4]$ is the Stefan-Boltzmann constant, $T_{\text{ref}} = 80$ k is the considered cryostat thermal shield temperature, and A/V is the surface-to-volume ratio of the object.

The heat deposited by the charged particle has the characteristic profile along the path showing the Bragg peak near the implantation region. The profiles for the α and ^7Li particles used in this simulation were evaluated by using the SRIM software [50]. The cold finger interface facing the helium flow is fixed at the operating temperature, while the initial temperature accounts also for the contribution of Q_J and Q_{irr} prior to the particle impact.

B. Electric Model

The electrical analysis takes into account current conservation based on the Ohm's law (i.e., neglecting the inductive effects), and implements an experimental resistivity, $\rho(T)$. Based on these assumptions, a known current source is injected into the Nb bridge by using two terminals, and the voltage drop is evaluated over the distance L between the voltage taps

$$\nabla_t \cdot d \left(\frac{1}{\rho} \nabla_t V - \mathbf{J_e} \right) = dQ_J. \tag{2}$$

In (2), d is the shell thickness, ρ is the electrical resistivity, V is the scalar potential–which tangential gradient defines the electric field $\mathbf{E}$ along the shell, and $\mathbf{J_e}$ and Q_J stands for the externally generated current density in the conducting material and the external current source, respectively.

IV. Model Validation

A first comprehensive analysis is intended to compare the model and the experimental results. Fig. 2 shows the time evolution of V for a sample with w = 10 μm and L = 600 μm.

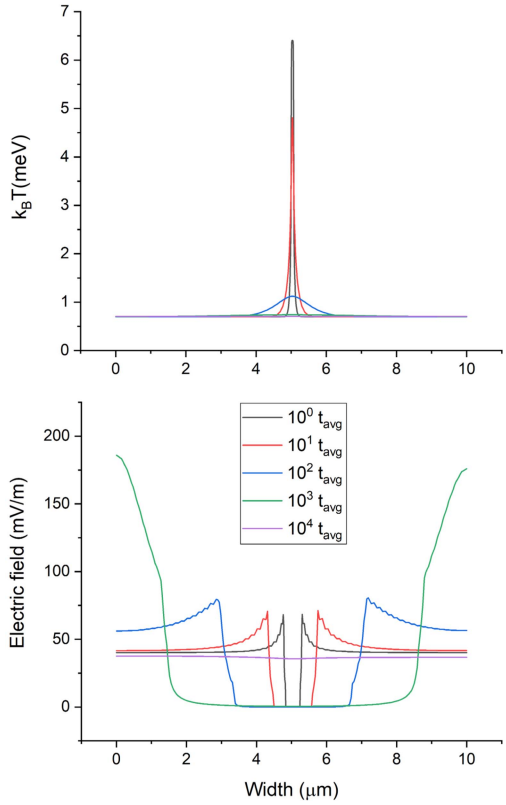

Fig. 3. Time evolution of the maximum local thermal energy in the Nb layer (up) and, for the same times, the electric field distribution (down) across the sample width.

In both experiments and simulations the cold finger temperature was kept at T = 8.12 K and the sample biased with a current I = 4.5 mA. The absence of a current diverting resistance, together with the chosen operating condition, induces the Joule self-heating of the resistive domain to expand over the whole strip length and produce a positive electro-thermal feedback (ETF). Indeed, both the measured (upper panel of Fig. 2) and the simulated (lower panel of Fig. 2) voltage signals revealed a latching state of about 150 mV until the current is switched-OFF. Also the time delay covered by the boundaries of the initial resistive region to propagate to the ends of the film - which is of the order of tens of μs in the present and described by the t_{onset} of the voltage drop in the lower panel of Fig. 2–depends on the electro-thermal cycle of the system (including the thermal contact resistances). To better support this, the trace of the quench dynamics in terms of the imparted energy and its tight interconnection with the electric field profile is plotted in Fig. 3.

The femtosecond particle interaction time-scale cannot be directly described with reference to the equilibrium temperature unless considering more sophisticated models [51]; conversely, the energetic description provides a clear qualitative understanding on the superconductivity depression. Fig. 3 is related to the interaction with ^{7}Li, which has an average time-of-flight (t_{avg} in the figure) of about 0.56 ps. A ns-range is required for the imparted energy to spread apart over the entire sample width and break the electric field symmetry. In the same time the electronic bath is thermalized with the sublattice ($\tau_{\text{e-p}} \sim 330$ ps) and the mean temperature starts increasing together with the electrical resistivity, while the normal zone expands along the Nb length. Fig. 2 highlights the average temperature of the superconducting volume between the voltage contacts. The chosen bias current makes the thermal sink ineffective and brings the temperature far above the material critical temperature.

V. Self-Recovering Option

In order to design a continuously working particle counting device, the simplest approach is to modify the operating conditions to reverse the ETF and allow self recovery. In other words, one can choose the conditions that modify the device timescales in such a way that either the Joule self-heating is reduced or the extracted power per unit input power is increased. Since both the bias current and the cold finger temperature also affect the figures of merit of the apparatus, the simplest approach is to find an experimentally feasible condition which allows self recovery while preserving as much as possible its responsivity (r) [53] and noise-to-equivalent power (NEP) [54].

The estimation of these over a broad range of values can be obtained from the following:

$$r = \frac{I}{G - I^2 \cdot \frac{\partial R}{\partial T}} \cdot \frac{\partial R}{\partial T} \tag{3}$$

$$\text{NEP} = \text{NEP}_J + \text{NEP}_t$$

$$\text{NEP}_J = \frac{4\kappa_B T R}{r^2}$$

$$\text{NEP}_t = 4\kappa_B T^2 G. \tag{4}$$

Here, I is the bias current, G is the substrate conductance, and $\frac{\partial R}{\partial T}$ is the electrical resistance curve slop as a function of temperature. NEP_J stands for the Johnson noise voltage, while NEP_t accounts for the noise power due to thermal fluctuation.

In Fig. 4, the calculated responsivity and NEP are presented as a function of the two operational variables. It is clear that, while the responsivity has a nonlinear dependence on temperature and a linear response in current, the NEP has a less obvious behavior being also affected by the inverse squared of the responsivity itself. However, the strong effect caused by the temperature is mostly related to the dR/dT shape; indeed, the materials properties remain almost constant in the considered temperature range.

As a result, reducing the transport current is more effective than reducing the cold finger temperature to reverse the ETF, and less impacting on the figure of merits. For instance, decreasing the current to a value of 3.6 mA, the responsivity is only slightly reduced to 1.9 mV $\cdot$ W^{-1} (with respect the 2.3 mV$\cdot$W^{-1} in the original case) and the NEP slightly increased to 6.7×10^{-15} W$\cdot$Hz$^{-1/2}$ (with respect the 4.3×10^{-15} W$\cdot$Hz$^{-1/2}$ in the original case), while the particle-assisted vortex motion self-contracts on a μs time-scale, restoring superconductivity (see Fig. 5).

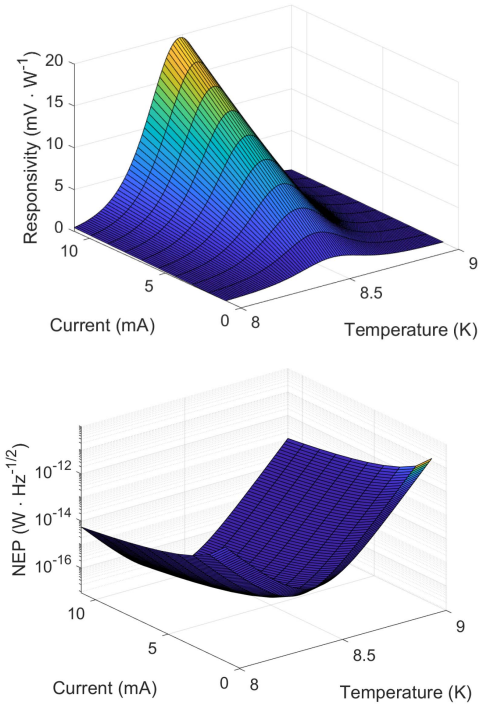

Fig. 4. Responsivity (up) and NEP (down on log scale) profiles over a broad range of cold finger temepratures and bias currents.

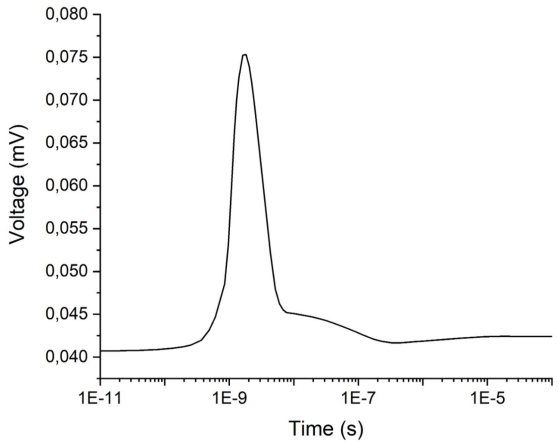

Fig. 5. Improved V-t simulation results for continuous particle detection.

VI. Conclusion

The finite element modeling turned out to be a valuable tool to characterize and evaluate the performance of superconducting neutron detectors. The dynamic response to single particle radiation has been obtained by considering both time and spatial evolution of temperature and current. The model has been validated against experimental data, the figures of merit have been estimated, and the operating conditions improved finding a self-recovery configuration. Notwithstanding the limits of the classical approach—which requires a critical thinking on the properties definition on very short time-scales—the results of this analysis well agree with the experimental data and are comparable with other data present in literature. This allows to get a reliable description of the apparatus with a computationally effortless model.

References

[1] A. Pietropaolo et al., "Neutron detection techniques from μeV to GeV," *Phys. Rep.*, vol. 875, pp. 1–65, 2020.
[2] A. K. Drukier et al., "A new detector of neutrons," *Nucl. Instrum. Methods*, vol. 154, pp. 91–94, 1978.
[3] G. Meagher et al., "Neutron detection using a planar array of superheated superconductors," *Nucl. Instrum. Methods Phys. Res. A*, vol. 230, pp. 8–10, 1996.
[4] T. Ebisu et al., "Cryogenic detection of neutrons using superheated superconducting tin granules," *Nucl. Instrum. Methods Phys. Res. A*, vol. 503, pp. 589–594, 2003.
[5] K. Takahashi et al., "Design of neutron detector by using a novel superconductor MgB_2," *Phys. C*, vol. 392–396, pp. 1501–1503, 2003.
[6] M. Machida et al., "Large-scale numerical simulations for superconducting neutron detector using MgB_2 and half quantized vortices in d-dot array," Annual Report of the Heart Simulator Center, Apr. 2003–Mar. 2004.
[7] T. Ishida et al., "Superconducting radiation detector by using a microfabricated MgB_2 meander line," *Phys. C*, vol. 460–462, pp. 618–619, 2007.
[8] T. Ishida et al., "Superconducting MgB_2 thin film detector for neutrons," *J. Low Temp. Phys.*, vol. 151, pp. 1074–1079, 2008.
[9] T. Ishida et al., "Position dependent response of superconducting MgB_2 neutron detectors studied by pulsed laser irradiation," *J. Low Temp. Phys.*, vol. 167, pp. 447–454, 2012.
[10] M. Nishikawa et al., "Numerical simulation for thermal relaxation of hot spot in MgB_2 neutron detector," *Phys. C*, vol. 463–463, pp. 1115–1118, 2007.
[11] M. Machida et al., "Direct numerical simulations for non equilibrium superconducting dynamics at the transition temperature edge: Simulation for MgB_2 neutron detectors," *J. Low Temp. Phys.*, vol. 151, pp. 58–63, 2008.
[12] M. Machida et al., "Ultra-large scale simulations for superconductor MgB_2 device toward nuclear application and fundamental issues in nanostructured superconductors," Annual Report of the Heart Simulator Center, Apr. 2007–Mar. 2008.
[13] M. Machida et al., "Numerical experiments for heat diffusion and related non-equilibrium superconducting dynamics on MgB_2 neutron detector," *Nucl. Instrum. Methods Phys. A*, vol. 600, pp. 210–212, 2009.
[14] V. Merlo et al., "Hybrid superconducting neutron detectors," *Appl. Phys. Lett.*, vol. 106, 2015, Art. no. 113502.
[15] V. Merlo et al., "Superconducting thermal neutron detectors," *J. Phys.: Conf. Ser.*, vol. 746, 2016, Art. no. 012019.
[16] V. Merlo et al., "Meta-material for nuclear particle detection," *J. Phys.: Conf. Ser.*, vol. 50, 2017, Art. no. 045601.
[17] V. Merlo et al., "Superconducting strips: A concept in thermal neutron detection," *Instruments*, vol. 2, 2018, Art. no. 2010004.
[18] H. Shishido et al., "Neutron detection using a current biased kinetic inductance detector," *Appl. Phys. Lett.*, vol. 107, 2015, Art. no. 232601.
[19] S. Miyajima et al., "Time-dependent flux from pulsed neutrons revealed by superconducting NB current-biased kinetic inductance detector with ^{10}B converter operated at 4k," *JPS Conf. Proc.*, vol. 8, 2015, Art. no. 051004.
[20] Y. Narukami et al., "Signal from a single neutron by using current-biased kinetic inductance detector made of superconducting NB nanowire," *JPS Conf. Proc.*, vol. 8, 2015, Art. no. 051003.
[21] H. Shishido et al., "Neutron detection using the superconducting NB-based current-biased kinetic inductance detector," *Supercond. Sci. Technol.*, vol. 3, 2017, Art. no. 094003.
[22] H. Shishido et al., "High-speed neutron imaging using a current-biased delay-line detector of kinetic inductance," *Phys. Rev. Appl.*, vol. 10, 2018, Art. no. 044044.
[23] Y. Iizawa et al., "Physical characteristics of delay-line current-biased kinetic inductance detector," *IOP Conf. Series: J. Phys.: Conf. Ser.*, vol. 1054, 2018, Art. no. 012056.
[24] Y. Miki et al., "Neutron signal features of NB-based kinetic inductance detector with ^{10}B convertor," *IOP Conf. Ser.: J. Phys.: Conf. Ser.*, vol. 1054, 2018, Art. no. 012054.
[25] Y. Iizawa et al., "Energy-resolved neutron imaging with high spatial resolution using a superconducting delay-line kinetic inductance detector," *Supercond. Sci. Technol.*, vol. 32, 2019, Art. no. 125009.

[26] T. D. Vu et al., "Kinetic inductance neutron detector operated at near critical temperature," *J. Phys.: Conf. Ser.*, vol. 1590, 2020, Art. no. 012036.
[27] H. Shishido et al., "Energy-resolved neutron imaging using a delay line current-biased kinetic-inductance detector," *J. Phys.: Conf. Ser.*, vol. 1590, 2020, Art. no. 012033.
[28] T. Ishida et al., "Superconducting neutron detectors and their application to imaging," *IEICE Trans. Electron.*, vol. E103–C, no. 5, pp. 198–203, May 2020.
[29] T. D. Vu et al., "Homogeneity of neutron transmission imaging over a large sensitive area with a four-channel superconducting detector," *Supercond. Sci. Technol.*, vol. 34, 2021, Art. no. 015010.
[30] T. D. Vu et al., "Practical tests of neutron transmission imaging with a superconducting kinetic-inductance sensor," *Nucl. Inst. Methods Phys. Res. A*, vol. 1006, 2021, Art. no. 165411.
[31] H. Shishido et al., "High spatial resolution neutron transmission imaging using a superconducting two-dimensional detector," *IEEE Trans. Appl. Supercond.*, vol. 31, no. 9, Dec. 2021, Art. no. 2400505.
[32] H. Shishido et al., "Neutron imaging for intermetallic alloy using a delay line current-biased kinetic-inductance detector," *J. Phys.: Conf. Ser.*, vol. 1975, 2021, Art. no. 012023.
[33] T. D. Vu et al., "Narrow-area Bragg-edge transmission of iron samples using superconducting neutron sensor," *J. Phys.: Conf. Ser.*, vol. 2323, 2022, Art. no. 012028.
[34] H. Shishido et al., "Neutron imaging toward epithermal regime using a delay line current-biased kinetic-inductance detector," *J. Phys.: Conf. Ser.*, vol. 2323, 2022, Art. no. 012029.
[35] M. Brock et al., "Superconducting transition edge bolometer for high–flux neutron detection," *Sci. Rep. Nature Portfolio*, vol. 13, 2023, Art. no. 22266.
[36] M. Brock et al., "Effective thermal properties of a HTS transition edge bolometer for high-flux neutron detection," *Adv. Electron. Mater.*, vol. 10, 2024, Art. no. 2300420.
[37] K. Boretzky et al., "NeuLAND: The high-resolution neutron time-of-flight spectrometer for R3B at FAIR," *Nucl. Inst. Methods Phys. Res. A*, vol. 1014, 2021, Art. no. 165701653.
[38] S. V. Afanas'ev et al., "The time resolution of a prototype neutron detector," *Instrum. Exp. Techn.*, vol. 59, no. 5, pp. 653–657, 2016.
[39] A. Tengattini et al., "Compact and versatile neutron imaging detector with sub-4 μm spatial resolution based on a single-crystal thin-film scintillator," *Opt. Exp.*, vol. 30, no. 9, pp. 14461–14477, 2022.
[40] G. Albani "High-rate thermal neutron gaseous detector for use at neutron spallation sources," Tesi di dottorato, Università degli Studi di Milano-Bicocca, 2017.
[41] S. Cancelli et al., "Development of a multi-layer high-efficiency GEM-based neutron detector for spallation sources," *Sci. Rep.*, vol. 14, 2024, Art. no. 23954, [Online]. Available: https://doi.org/10.1038/s41598-024-74958-5
[42] C. Petrillo et al., "Solid state neutron detectors," *Nucl. Instrum. Methods Phys. Res. Sect. A: Accelerators, Spectrometers, Detectors Assoc. Equip.*, vol. 378, no. 3, pp. 541–551, 1996.
[43] K. Ahmed et al., "Solid-state neutron detectors based on thickness scalable hexagonal boron nitride," *Appl. Phys. Lett.*, vol. 110, 2017, Art. no. 023503, [Online]. Available: https://doi.org/10.1063/1.4973927
[44] K. Toh et al., "Performance evaluation of high-pressure MWPC with individual line readout under Cf-252 neutron irradiation," *J. Phys.: Conf. Ser.*, vol. 528, 2014, Art. no. 012045.
[45] M. Angelone and C. Verona, "Properties of diamond-based neutron detectors operated in harsh environments," *J. Nucl. Eng.*, vol. 2, pp. 422–470, 2021, [Online]. Available: https://doi.org/10.3390/jne2040032
[46] Y. Lee et al., "Diamond fast-neutron detector applied to the KSTAR tokamak," *Fusion Eng. Des.*, vol. 153, 2020, Art. no. 111452.
[47] M. Pérez et al., "Thermal neutron detector based on COTS CMOS imagers and a conversion layer containing gadolinium," *Nucl. Inst. Methods Phys. Res. A*, vol. 893, pp. 157–163, 2018.
[48] V. Merlo, "Superconducting strips: A concept in thermal neutron detection," *MDPI J. Instrum.*, vol. 2, 2018, Art. no. 4.
[49] *COMSOL Multiphysics*, COMSOL AB, Stockholm, Sweden. [Online]. Available: www.comsol.com
[50] J. F. Ziegler, M. D. Ziegler, and J. P. Biersack, "SRIM – The stopping and range of ions in matter." *Nucl. Instrum. Methods Phys. Res. Sect. B: Beam Interact. Mater. At.*, vol. 268, no. 11, pp. 1818–1823, 2010, doi: 10.1016/j.nimb.2010.02.091.
[51] J. W. Yin et al., "Heat transfer in superconducting nanowire single-photon detectors: Mechanism and modulation," *Sci. Technol. Supercond.*, vol. 37, 2024, Art. no. 073001, [Online]. Available: https://doi.org/10.1088/1361-6668/ad54f2
[52] A. Napolitano et al., "Study of the thermal distribution for YBCO based transition edge bolometers working above 77 k," in *Proc. IEEE 14th Workshop Low Temp. Electron.*, Matera, Italy, 2021, pp. 1–4, doi: 10.1109/WOLTE49037.2021.9555450.
[53] M. K. Maul et al., "Equivalent circuit of a superconducting bolometer," *J. Appl. Phys.*, vol. 40, 1969, Art. no. 2822, doi: 10.1063/1.1658082.
[54] J. C. Mather et al., "Bolometer noise: Nonequilibrium theory," *Appl. Opt.*, vol. 21, no. 6, pp. 1125–1129, 1982.

Open Access funding provided by 'Politecnico di Torino' within the CRUI CARE Agreement